Acta Materialia 179 (2019) 224–236

Contents lists available at ScienceDirect

Acta Materialia

journal homepage: www.elsevier.com/locate/actamat

Full length article

In situ characterization of a high work hardening Ti-6Al-4V prepared by electron beam melting

K. Sofinowski [a, b], M. Šmíd [a], I. Kuběna [a, c], S. Vivès [d], N. Casati [e], S. Godet [d], H. Van Swygenhoven [a, b, *]

[a] Photons and Engineering for Manufacturing, Paul Scherrer Institut, CH-5232, Villigen, Switzerland
[b] Neutrons and X-rays for Mechanics of Materials, IMX, École Polytechnique Fédérale de Lausanne, CH-1012, Lausanne, Switzerland
[c] CEITEC IPM, Institute of Physics of Materials AS CR, V.v.i., Žižkova 22, 616 62, Brno, Czech Republic
[d] 4MAT, Université Libre de Bruxelles, CP165/63, Avenue F.D. Roosevelt 50, 1050, Bruxelles, Belgium
[e] Laboratory for Synchrotron Radiation – Condensed Matter, Paul Scherrer Institut, CH-5232, Villigen, Switzerland

ARTICLE INFO

Article history:
Received 7 February 2019
Received in revised form
12 August 2019
Accepted 20 August 2019
Available online 21 August 2019

Keywords:
Titanium alloy
Additive manufacturing
In situ tension test
X-ray diffraction (XRD)
Digital image correlation

ABSTRACT

A multi-phase Ti–6Al–4V prepared by electron beam melting and thermal post treatments has been shown to exhibit increased strength and ductility over standard wrought or hot isostatic pressed Ti–6Al–4V. The mechanical improvements are due to a prolonged, continuous work hardening effect not commonly observed in Ti alloys. *In situ* x-ray diffraction and high resolution digital image correlation are used to examine the strain partitioning between the phases during tensile loading with post-mortem electron microscopy to characterize the deformation behavior in each phase. Specimens heat treated between 850 and 980 °C were tested and the effect of annealing temperature on the micromechanical response is discussed. It is shown that the work hardening is the result of composite load-sharing behavior between three mechanically distinct microstructures: large α lamellae and a martensitic region of fine acicular α' and a third phase not previously reported in this alloy.

1. Introduction

Titanium alloys, Ti–6Al–4V in particular, have found widespread use in the aerospace and biomedical fields due to their excellent strength-to-weight ratio, corrosion resistance, and biocompatibility [1–7]. However, the relatively low work hardening and ductility of the alloys in comparison to other metals like steels still restricts their usage [8,9]. The desire for Ti alloys with increasingly optimized combinations of strength and ductility has led to the development of alloys with increasingly complex multi-phase microstructures [3,10]. By tailoring the phase fractions and morphologies, different balances of strength, ductility, and work-hardening can be achieved.

Generally, a combination of thermo-mechanical processes is used to optimize the microstructure. For example, various thermal forming and annealing techniques have been applied to dual-phase $\alpha+\beta$ Ti–6Al–4V to create bi-modal grain distributions that balance strength and ductility [11–15]. Post-processing routes for additive manufactured (AM) parts, however, cannot use mechanical processes to control grain size or morphology because the printed parts are already near their final shape. Thus, thermal-only post-processing routes are being explored to tailor new microstructures in AM parts [16,17].

Recently, de Formanoir et al. applied a novel heat treatment to generate a dual-phase $\alpha+\alpha'$ microstructure in a Ti–6Al–4V prepared by electron beam melting (EBM) [18]. The alloy showed both higher ultimate tensile strength (UTS) and ductility as-compared to standard wrought or hot-isostatic pressed (HIP'ed) samples. The improved mechanical properties were attributed to a composite work-hardening behavior between the α and α' phases. The α' phase is generally considered to be an unwanted brittle phase and is usually decomposed to $\alpha+\beta$ [19–23]. However, recent studies were able to achieve high ductilities in a fully α' -martensitic [24] and $\alpha+\alpha'$ dual-phase [25,26] Ti–6Al–4V, challenging the conventional idea that the martensite is inherently brittle.

In this study, the source of the work hardening behavior of a Ti–6Al–4V alloy prepared by EBM and post heat treatments similar to those performed by de Formanoir et al. [18] is determined during

* Corresponding author. Photons and Engineering for Manufacturing, Paul Scherrer Institut, CH-5232, Villigen, Switzerland.
E-mail address: helena.vs@psi.ch (H. Van Swygenhoven).

https://doi.org/10.1016/j.actamat.2019.08.037

uniaxial tensile loading. It is shown that the high work hardening is due to the composite behavior of three mechanically distinct phases: α lamellae and martensitic regions containing acicular laths of α' and a third phase which has not been identified in literature. The load sharing between the three phases is investigated *in situ* with x-ray diffraction (XRD) and high resolution digital image correlation (HRDIC) and the implications on hardening mechanisms within the phases are discussed.

2. Experimental procedure

2.1. Material

Blocks of Ti–6Al–4V were prepared by EBM using an Arcam AB® A2 machine with the standard ARCAM melting parameters. The chemical composition of the powder used is shown in Table 1. To reduce the number of macroscopic defects inherent to the EBM process, the blocks were subjected to hot isostatic pressing (HIP) for 2 h at a pressure of 1000 bar and temperature 920 °C followed by slow cooling in a furnace. After HIP, 300 μm thick sheets were cut from the block. The sheets were encapsulated in quartz tubes under an argon atmosphere, to avoid oxidation, and annealed for 2 h at four different sub-transus temperatures (850, 900, 950 and 980 °C) to produce different proportions of α/β. Immediately after annealing, the sheets were water quenched (WQ) to transform the β phase into martensite. For more details on the EBM process and subsequent post-treatments we refer to Ref. [18].

For *in situ* XRD, flat dogbone specimens were cut from the sheets by wire electro-discharge erosion and then polished by mechanical grinding to remove surface defects. After polishing, the gauge section dimensions were 1.25 mm wide and between 270 and 290 μm thick. It should be noted that shallow notches developed at the edges of the gauge section of the XRD samples during polishing. Strain concentrations developed at these notches and resulted in the premature failure of the 850C, 900C, and 950C heat-treated samples.

In situ HRDIC dogbones were cut using picosecond-pulsed laser ablation at the Swiss Federal Laboratories for Materials Science and Technology (EMPA). The samples were then mechanically ground using SiC sandpaper with decreasing roughness (320, 600, 800, and 1200 grit) then polished with 3 μm and 1 μm diamond paste. The final gauge sections were 300 μm wide and between 67 and 80 μm thick. Final polishing was performed using an OPS suspension for 45 min to achieve a mirror-like surface.

2.2. In situ x-ray diffraction (XRD)

XRD spectra were recorded *in situ* during continuous tensile loading (initial strain rate 0.0001 s^{-1}) using a miniaturized tensile machine mounted at the Materials Science beam line at the Swiss Light Source [27]. Samples were measured in transmission using a 20 keV beam of 200 × 500 μm^2. Diffraction patterns were acquired every 20 s with a Mythen II microstrip detector with the diffraction vector **Q** perpendicular to the loading direction. During each diffraction pattern, the machine was rotated ± 6° about the loading axis to increase grain statistics. A PixelLink camera (P-DL729MU) with inline 2 × telecentric lens (Edmund Optics, model #67313) mounted above the sample was used to capture images for DIC analysis. The strain values reported in this study are averaged over the irradiated section of 200 × 500 μm^2.

Diffraction peaks are fit using a split Pearson VII function and the peak position, peak width (full-width at half-maximum – FWHM), and peak intensity are extracted. The evolution of the elastic lattice strains is calculated from the change in peak position of a given $\{hk.l\}$ reflection ($\varepsilon_{hk.l} = (d_{hk.l} - d^0_{hk.l})/d^0_{hk.l}$) and can be used to examine load sharing between different grain families [28]. A positive change in slope of $\varepsilon_{hk.l}$ vs. applied stress implies that grain family $\{hk.l\}$ is taking more load, whereas a negative change in slope implies that it is taking less load ("shedding load"). Changes in the FWHM correlate to changes in the dislocation density within grains or intergranular stress inhomogeneity within a grain family.

Table 1
Chemical composition (wt. %) of the Arcam Ti–6Al–4V powder used in the EBM process (from Ref. [18]).

	Al	V	C	Fe	O	N	H	Ti
Arcam Ti–6Al–4V	6	4	0.03	0.10	0.15	0.01	0.003	Balance

2.3. In situ high resolution digital image correlation

Dogbones were prepared with one of two types of speckle patterns to perform HRDIC at different magnifications: colloidal silica – OPS (low magnification) or gold speckles (high magnification). The OPS pattern was prepared by dispersing dilute OPS polishing suspension on the surface of the dogbone using the methods in Ref. [29]. The resulting pattern consisted of a semi-random distribution of ~61 nm diameter speckles with an average inter-speckle distance of 175 nm. The gold speckle pattern was prepared by remodelling a thin layer of gold deposited on the surface of the dogbone as in Refs. [30,31]. The gold speckles had an average diameter of 17 nm with an average inter-speckle distance of 22 nm. After patterning, EBSD micrographs were collected using a Zeiss ULTRA 55 FEG scanning electron microscope (SEM). Maps were taken with step sizes between 80 and 120 nm (20 kV, high current mode, 120 μm aperture). Raw data was post-processed using OIM Analysis 7.3 software.

Interrupted tensile load tests were performed using one axis of a miniaturized biaxial machine (described in Ref. [32]) mounted inside of a FEG Zeiss ULTRA 55 SEM. Dogbones were loaded in tension at a constant total strain rate $\dot{\varepsilon}_{tot} = 0.00014$ s^{-1} to five predetermined force levels. At each level, the dogbone was held under constant displacement to avoid extensive creep during SEM image acquisition. During the hold the stress relaxes. Thus, a delay of 5 min was included to allow the sample to relax before image acquisition began. A series of four SEM images were taken at each force level during a period of ~40 min. During this time, the stress did not drop more than 4 MPa.

High contrast grayscale images were obtained using conditions described by Yan et al. [29]: an in-lens detector was used at a working distance of 7 mm with acceleration voltage of 3 kV and an aperture size of 30 μm. The images were stitched together to form a 2 × 2 grid with dimensions of 108 μm × 81 μm (OPS sample) or 16 μm × 12 μm (gold-speckle sample). Each image had a resolution of 3072 x 2304 pixels. This resulted in an average speckle diameter and inter-speckle distance of 5 and 10 pixels, respectively, for the OPS pattern, and 5 and 7 pixels, respectively, for the gold pattern. Strain maps were calculated from the grayscale images using the open source 2D DIC Matlab software Ncorr [33]. For both the OPS and gold patterned-samples, a subset radius of 15 pixels, subset spacing of 3 pixels, and strain radius of 3 pixels was used. The minimum subset radius for the DIC software to correctly track the subsets was found to be ~8 pixels due to the pattern density and distribution, while a maximum radius of 77 pixels was set by the software. Low values were used for the subset radius and strain radius to optimize spatial resolution [29,34], although this increases the strain noise locally. Therefore, a subset radius of 15 pixels was chosen to maximize spatial resolution without

introducing a large effect from the signal-to-noise ratio.

A dogbone was strained *ex situ* to correlate macrostrain values with the piezo motor steps because the displacement of the arms could not be directly measured *in situ* due to the size constraints of the SEM chamber. Unlike the *in situ* tests, the *ex situ* test was continuous. Thus, it is expected that the actual macrostrain values of the *in situ* tests are slightly higher than shown due to creep during the HRDIC imaging.

2.4. Electron microscopy techniques

Pre- and post-mortem SEM and TEM was performed to characterize the microstructure of the material. TEM lamellae were prepared by focused ion beam (FIB) milling using a Zeiss NVision-40 FEG-SEM. TEM and selective area electron diffraction (SAED) were performed using a JEOL JEM-2100F TEM (Institute of Physics of Materials, Brno) and a JEOL JEM 2010 TEM (Paul Scherrer Institute). Transmission Kikuchi diffraction (TKD) was performed using a Tescan LYRA 3 XMU FEG-SEM (IPM, Brno) and the patterns were indexed using Oxford Instruments Aztec software.

3. Results

3.1. Material characterization

3.1.1. Microstructure

The microstructure of all heat treated samples consists of large α lamellae surrounded by regions of martensite. The martensite volume fraction was estimated from the area fraction measured from EDX V- and Al- element micrographs following the procedure outlined by de Formanoir et al. [18]. The phase fractions were measured to be: 850 °C—25 ± 4%, 900 °C—34 ± 4%, 950 °C—48 ± 4%, and 980 °C—58 ± 4%. These values are systematically lower than those reported by de Formanoir et al. [18]. This can be attributed to slightly faster cooling rates during the transfer to the water quench because the samples were thinner.

The α lamellae are approximately 2—4 μm wide and 10—20 μm long and form a "basket-weave" microstructure typically seen in α/β alloys [35,36]. Individual lamellae are either single grain or several grains with low misorientation angle grain boundaries. An inverse pole figure (IPF) map for the 900C sample is shown in Fig. 1a. The IPF is generated from an area three times larger than the map. In some areas large colonies of grains with the same orientation have formed due to a preferred orientation relationship with the parent β grain [15,35].

TEM micrograph and IPF map obtained by TKD (Fig. 1b and c) show that the martensite regions contain fine acicular α' approximately one order of magnitude smaller than the α lamellae. The α' laths exhibit a heavily twinned/faulted microstructure typical of Ti—6Al—4V martensite [19]. The laths appear to have no preferred crystallographic orientation (Fig. 1c), but are known to have a specific Burgers relationship to the parent β grains with 12 possible variants [37]. The seemingly "random" texture is likely due to the absence of preferred variant selection during the martensitic transformation. A large distribution of α' lath sizes is observed in all samples, but larger laths are observed in samples annealed at higher temperatures.

The lattice parameters of the α and α' HCP phases shown in Table 2 were calculated from the XRD patterns (Fig. 2a). During the anneal, Al and V partition to the α and β phase, respectively. The solute atoms are then trapped during the water quench, resulting in Al-enriched α lamellae and V-enriched martensite regions. The lattice parameters of the α' phase are systematically smaller than the α phase due to the larger mismatch between the size of the Al solute atoms and Ti. The effect of partitioning is visible in the increasing a and c lattice parameters of the α' and the c parameter of the α phase as the annealing temperature increases. The variation in initial peak intensities between the different heat treatments is suspected to be due to the limited number of diffracting grains as the crystallographic textures should be similar for all samples.

3.1.2. A third phase in the martensite region

Additional XRD reflections, marked by arrows in Fig. 2a, were observed in all un-strained samples. Two distinct peaks were observed for all heat treatments near $2\theta_{hk.l} = 24.2°$ and $2\theta_{hk.l} = 16.0°$. Additional peaks were observed as "shoulders" on α peaks in the 850C sample (shown in insets in Fig. 2a). As the α lamellae consist of large single grains (Fig. 1), the additional peaks should come from the martensite regions.

It was examined whether the peaks are due to a second set of α' grains under preferential residual stresses from the martensitic $\beta \rightarrow \alpha'$ transformation. It has been observed that the $\beta \rightarrow \alpha'$ transformation results in strong residual stress development due to the large orientation differences between adjacent α' laths [38]. However, the large difference in $2\theta_{hk.l}$ between the additional peaks and the α' peaks makes it highly unlikely that the shift can be explained by residual stresses alone. Considering the 900C sample, the additional peak in the initial XRD pattern at $2\theta_{hk.l} = 24.22°$ would correspond to the $\{11.0\}$ orientation. The residual elastic lattice strain, calculated directly from the difference in $2\theta_{hk.l}$ between this peak and $\{11.0\}$ α', would be 2.5%. Although the residual stress tensor cannot be measured by our diffraction setup, the elastic modulus along the (11.0) direction, $E_{11.0} = 96 - 105.5$ GPa [39], suggests a tensile residual stress on the order of 2.5 GPa, which is significantly higher than the UTS of the materials measured in this study (Fig. 3) and by de Formanoir et al. [18]. Similar calculations for the 850C, 950C, and 980C samples would give residual elastic lattice strains of 2.6%, 1.9%, and 1.5%, respectively. Therefore, it is much more likely that part of the peak shift is due to a chemical difference, i.e. the presence of a third phase not previously identified in this material (henceforth, "Phase-3").

The Phase-3 peaks can be indexed with either orthorhombic (OR) or HCP lattice parameters. Indexing as HCP (not considering residual stress) yields lattice parameters that decrease with increasing annealing temperature between $a = 2.956 \pm 1\text{e-}4$ Å and $c = 4.684 \pm 3\text{e-}4$ Å (850C sample) and $a = 2.945 \pm 4\text{e-}4$ Å and $c = 4.64 \pm 3\text{e-}2$ Å (980C sample). The error on the c parameter of the 980C sample is large compared to the 850C sample because there is significant uncertainty in the peak position due to the overlap between the peaks. Indexing Phase-3 as OR yields lattice parameters of $a = 2.956 \pm 9\text{e-}4$ Å, $b = 5.05 \pm 7\text{e-}4$ Å, and $c = 4.61 \pm 3\text{e-}2$ Å for the 850C sample. The OR parameters could not be calculated for the other heat-treated samples because the additional peaks are not distinctly visible in the un-strained XRD patterns.

To further characterize Phase-3, selected area electron diffraction (SAED) was performed on laths within the martensite region, i.e. regions which are not primary α lamellae (Fig. 2b and c). Circles show the size of the SAED apertures used to produce the diffraction pattern in Fig. 2d and e. The SAED pattern in Fig. 2d can be clearly indexed using the α' lattice parameters calculated from XRD, shown in Table 2. However, using smaller apertures, several laths were identified which could not be well-indexed by the α or α' lattice parameters. These laths are suspected to belong to Phase-3. The SAED pattern in Fig. 2e comes from the circled area marked "1" in Fig. 2c. Using the lattice parameters calculated from XRD, the spots can be indexed as either OR or HCP with a 3% and 30% indexing error, respectively.

In other words, XRD and SAED show the presence of a third phase, but cannot definitively determine its crystallographic

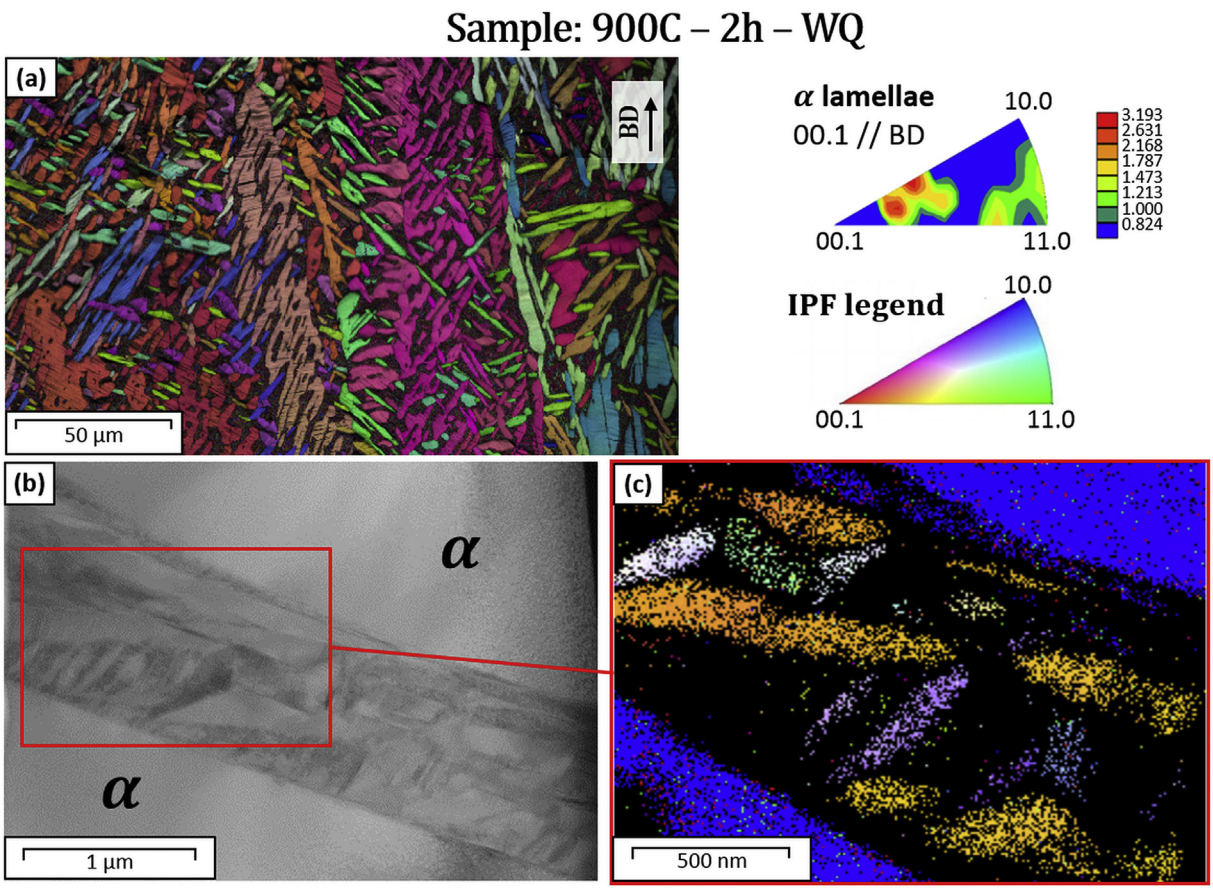

Fig. 1. Microstructure of the 900C sample: (a) IPF and IPF map (w.r.t the build direction) of the α lamellae surrounded by dark grey martensite; (b) TEM dark-field contrast micrograph of the martensite region between α lamellae; (c) IPF map from transmission kikuchi diffraction of the martensite region.

structure. Considering Phase-3 to be HCP implies that two chemically distinct α' martensites are formed during quenching, which has never been reported in literature, or that a secondary α forms in the martensite regions. Since Phase-3 diffracts at lower angles than the primary α and α' peaks, there must be differences in chemical composition and/or residual stresses. A secondary α phase, so-called α_m, has been observed in Ti–6Al–4V martensite as the result of a massive transformation at near-quench cooling rates [40]. However, the observed α_m had nearly identical chemistry and lattice structure to the α' martensite, so it is difficult to explain the large difference in XRD peak positions. Secondary α has also been previously observed as planar interface complexions in martensite [41], but such phenomena are known to be related to diffusion-controlled processes [42–44] and should not have occurred during a quench.

The small indexing error of the SAED spots, on the other hand, suggests that Phase-3 is OR α'' martensite. The lattice parameters are indeed similar to the α'' phase observed in Ti–6Al–6V–2Sn ($a = 2.95$ Å, $b = 5.00$ Å, and $c = 4.63$ Å). The phase forms as a distorted HCP structure at high β -stabilizer solute content, which explains its location in the martensite. This martensite has been reported in Ti–6Al–4V when quenching from starting temperatures of 800°C–900 °C [45], a temperature range through which all of the heat treatments in this study pass during the water quench. However, it has never been reported in combination with α' martensite.

In summary, more advanced methods are required to characterize the crystallography of Phase-3. It is suggested that atom probe tomography could potentially identify short-range chemical differences in the martensite regions that could not be identified by standard energy dispersive methods. Our study, however, focuses on explaining the enhanced work hardening observed in this Ti–6Al–4V due to the load sharing between the α, α', and Phase-3.

Table 2
Lattice parameters of the α and α' phases measured by synchrotron XRD.

Sample	**α lamellae**		α′ laths	
	a (Å)	*c* (Å)	*a* (Å)	*c* (Å)
850C-2h-WQ	2.928 ± 7e-6	4.675 ± 5e-3	2.881 ± 7e-4	4.647 ± 4e-2
900C-2h-WQ	2.928 ± 6e-6	4.678 ± 8e-6	2.883 ± 3e-4	4.654 ± 1e-4
950C-2h-WQ	2.929 ± 3e-6	4.686 ± 1e-5	2.894 ± 3e-3	4.659 ± 3e-4
980C-2h-WQ	2.927 ± 5e-5	4.686 ± 8e-5	2.899 ± 4e-4	4.659 ± 4e-4

3.1.3. Mechanical behavior

The true stress-strain curves until necking or fracture and the evolution of the work hardening exponent $n_{incr} = d\ln\sigma/d\ln\varepsilon$ are shown in Fig. 3. As in the study of de Formanoir et al. [18], the annealed samples show significant increases in work hardening and ultimate tensile strength as compared to the as-HIP'ed sample. The trends are also the same: as annealing temperature (and thus martensite region volume fraction) increases, 0.2% yield strength ($R_{p0.2}$) and ultimate tensile strength also increase. Unfortunately, stress concentrations outside of the gauge section caused the premature fracture of the 850C, 900C, and 950C samples at 4%, 5%, and 7%, respectively. Nevertheless, we believe that it is unlikely that new work hardening mechanisms will appear beyond 4–5% strain

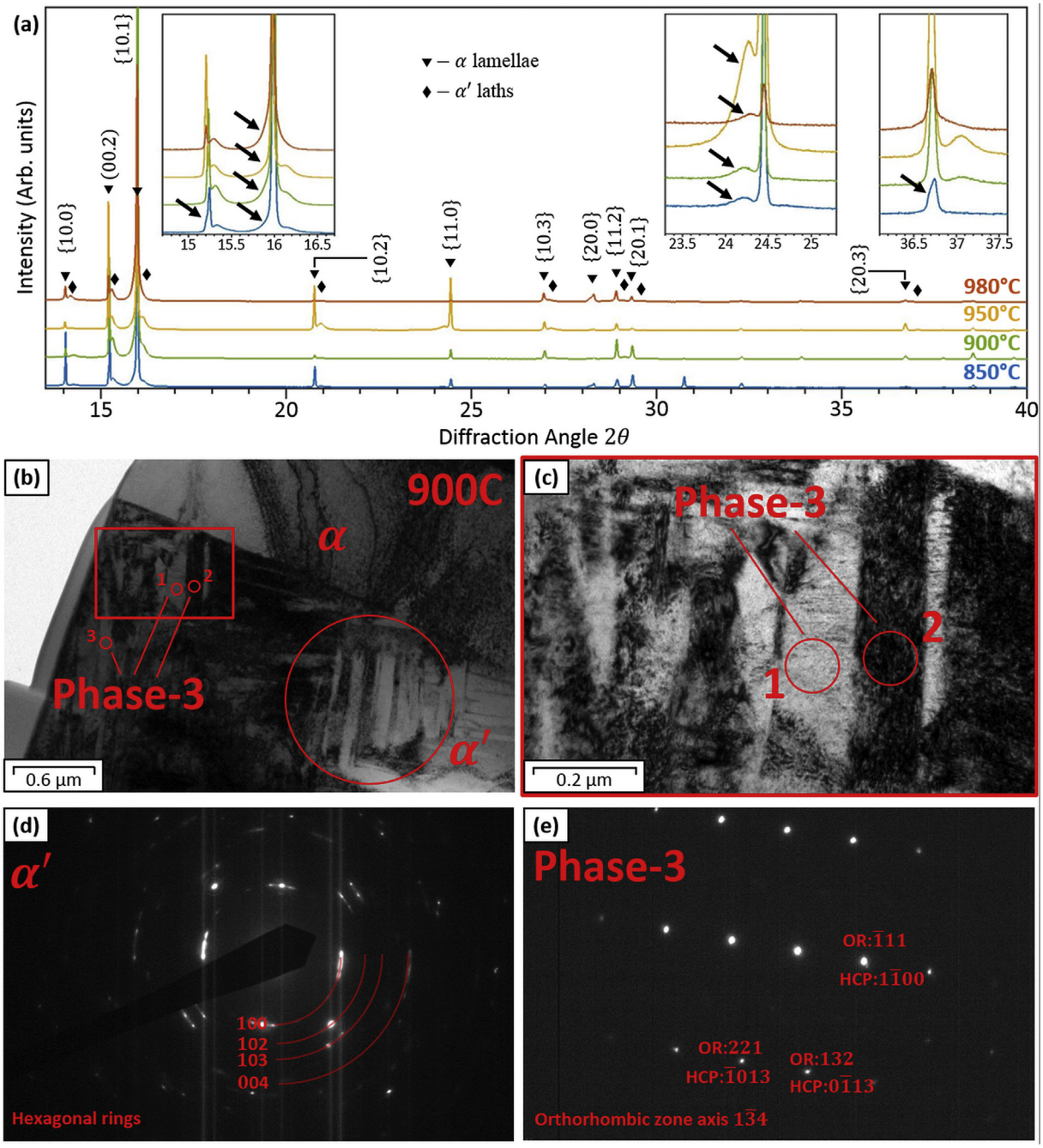

Fig. 2. (a) XRD profiles of the un-strained heat treated samples. Insets highlight scattering angles where Phase-3 peaks were observed; (b) TEM bright-field micrograph of martensite region showing the location of α, α', and Phase-3 identified by SAED; (c) Magnified view of suspected Phase-3 laths; (d) SADP of α' showing hexagonal rings; (e) SAED pattern of Phase-3 lath 1 from Fig. 2c, which can be indexed by either OR or HCP lattice parameters calculated from XRD.

so the behaviors observed here represent a complete picture of the work hardening in the material.

3.2. Deformation of the 900C sample

3.2.1. Load sharing between phases: In situ XRD

As the samples were deformed *in situ*, additional reflections of Phase-3 were observed near additional HCP reflections, as shown for example near the {10.2} reflection in Fig. 4. Initially, the XRD line profile can be well-described by two peaks, {10.2} α and α' (Fig. 4a). However, after ~650 MPa applied stress, it is not possible to fit the XRD profile with less than three peaks. As the deformation proceeds the peaks shift relative to one another due to the mechanical differences between the phases (Fig. 4 b,c). The full video of the evolution of the {10.2} and {11.0} reflections is available as supplementary material online.

It is clear that the Phase-3 peak near {11.0} α is present from the initial microstructure. On the other hand, the appearance of the third peak in Fig. 4 implies that this peak is either (i) present from the initial microstructure but overlapped by the {10.2} α peak, or (ii) appears during loading, e.g. by grains rotating into diffraction condition. Above 650 MPa, the three peaks evolve independently of one another, directly implying that they each belong to a mechanically distinct set of grains. It is suspected that these additional

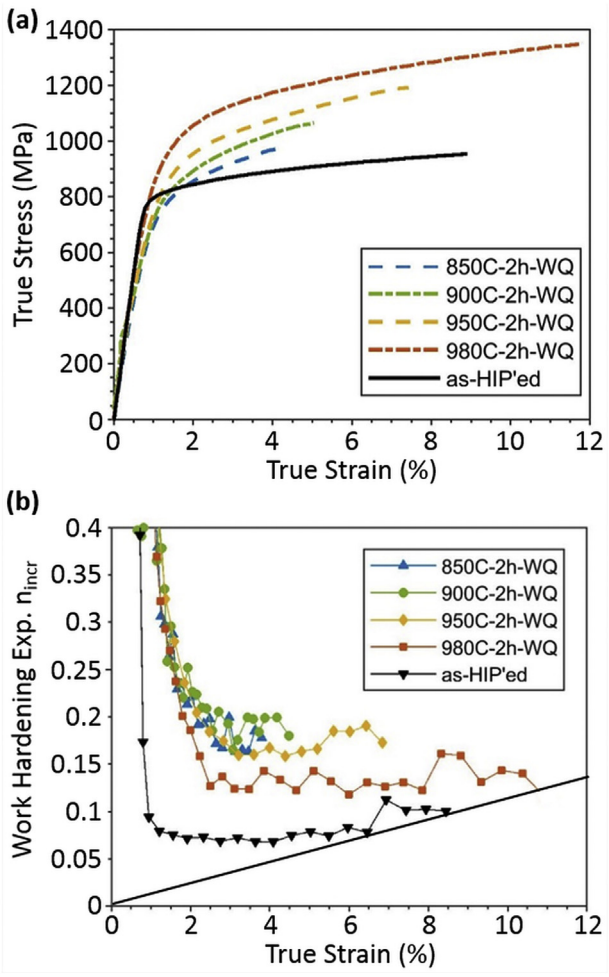

Fig. 3. (a) True stress, true strain curves until necking or fracture and (b) work hardening exponent n_{incr} as a function of the strain for the samples tested with *in situ* XRD. The cutoff line in (b) is Considere's criterion for necking.

peaks are Phase-3 peaks because of their similar mechanical behaviour to the {11.0} α peak.

The evolution of the elastic lattice strains ($\varepsilon_{hk.l}$) as a function of applied stress are shown in Fig. 5 for a few {*hk.l*} grain families of the three phases. Grain families having a peak position in a similar 2θ range are plotted together. As it is uncertain whether Phase-3 is OR or HCP, the Phase-3 grain families will be named as follows: P3.1, which could be either {11.0} secondary α or {200} α''; P3.2, which could be either {10.2} secondary α or {112} α''; and P3.3, which could be either {20.3} secondary α or {300} α''. The {10.1}, {20.0}, {11.2}, and {20.1} HCP reflections show significant overlap between α, α', and Phase-3 peaks in the initial microstructure so it is difficult to uniquely fit the peaks. The peak broadening (ΔFWHM) of the {10.0} α, {10.0} α', {11.0} α, and P3.1 grain families is shown in Fig. 6. The error bars for {11.0} α are too small to be shown ($\delta(\Delta FWHM) < \pm 0.001$). The elastic lattice strain and FWHM evolution in Figs. 5 and 6 are only shown as far as the diffraction peaks could be uniquely fit; i.e. depending on the reflection, they are not necessarily shown for the full loading.

The following can be deduced from the development of the elastic lattice strains and peak broadening of the three phases:

Elastic regime: Below applied stresses of ~300 MPa, $\varepsilon_{hk.l}$ changes linearly for all phases (Fig. 5), suggesting that all phases behave elastically.

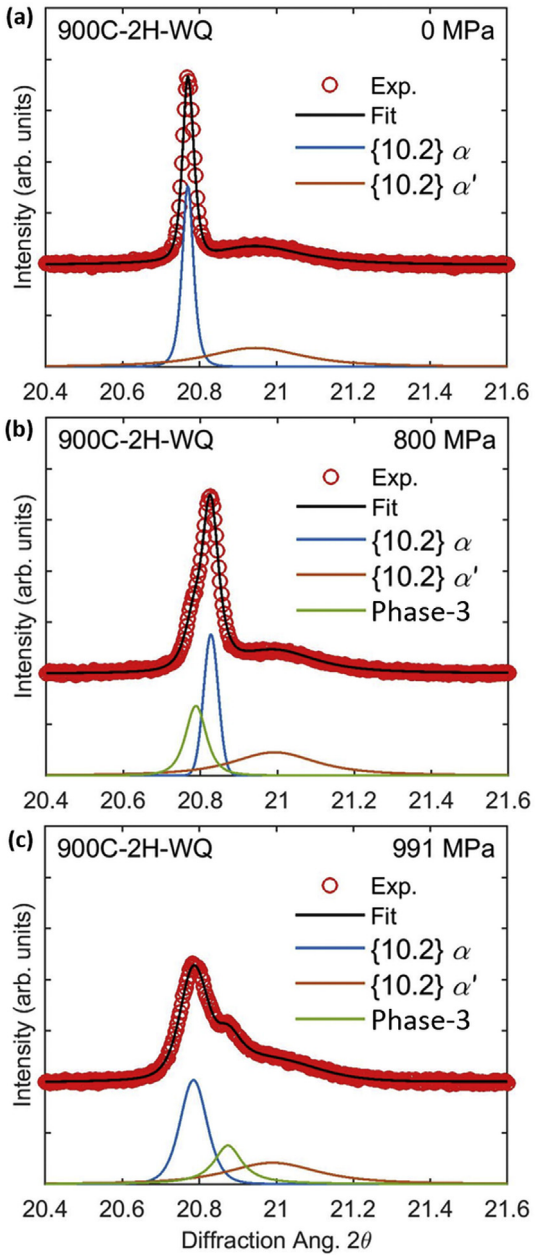

Fig. 4. Peak evolution of the 900C sample near the {10.2} HCP reflection (a) in the initial (unloaded) state, (b) just after macroplastic yield, and (c) at the end of loading.

Microplastic regime: Between ~300 MPa and $R_{p0.2} = 760$ MPa, α' and Phase-3 both seem to shed load, however with important differences: peak broadening is observed for the α' peaks (Fig. 6a) but not for Phase-3 peak P3.1 (Fig. 6b). This behavior can be explained by load sharing within the martensite region. As stress is applied, intergranular stresses are redistributed between the Phase-3 laths and some α' laths plastify. The lattice strain of some α reflections starts deviating before reaching $R_{p0.2}$, suggesting early plastification of some well-oriented grains. This is confirmed by the peak broadening e.g. in the {10.0} and {11.0} grain families in Fig. 6b.

Plastic regime: Above $R_{p0.2} = 760$ MPa, the α phase plastifies: some grain families shed load strongly, e.g. {10.2} and {20.3} (Fig. 5d and e), while other grain families continue to take load, e.g. {11.0} and {10.0} (Fig. 5b and c). Within the martensitic regions,

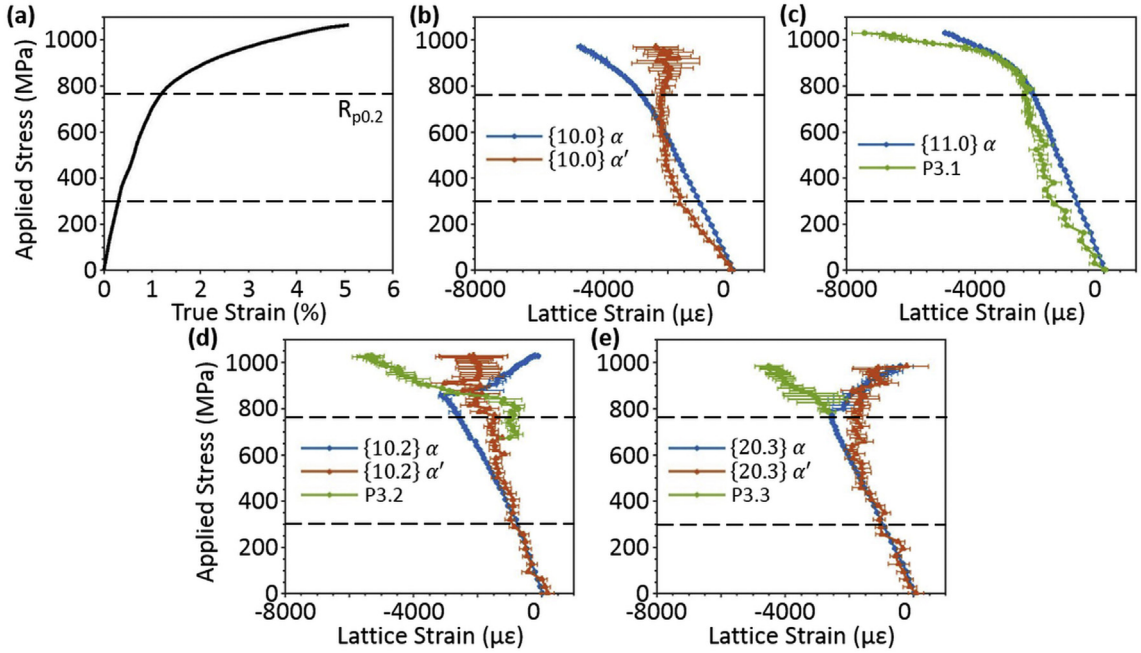

Fig. 5. (a) Applied stress, true strain curve and (b–e) lattice strain evolution of several grain families for the 900C sample. The same stresses are marked on each graph for comparison.

the α' laths do not take more load. Instead, the load is rapidly taken by Phase-3 (Fig. 5) accompanied by a rapid peak broadening (Fig. 6).

The α grain families that shed load in the plastic regime depends on which families are plastically "soft," i.e. which have the most grains deforming by low critical resolved shear stress (*CRSS*) slip mechanisms. While it is well understood that Ti–6Al–4V is plastically anisotropic, the relative strengths of the deformation mechanisms is currently under debate. Crystal plasticity simulations and electron microscopy studies [46–48] have estimated that *a* slip on prismatic planes (*Pria*) is the easiest, followed closely by basal *a* slip (*Baa*) with a $CRSS_{Baa}$ ~1.1 × higher than $CRSS_{Pria}$. By contrast, more recent studies by high-energy XRD suggest that *Baa* slip is the weakest system, with $CRSS_{Pria}$ ~1.1-1.2 × higher than $CRSS_{Baa}$ [49–51]. The activation of *a* slip on first-order pyramidal planes ($Pyr_{1st}a$) is considered third weakest, although its activity is debated to occur and many studies omit it altogether. However, all studies agree that *a* -type slip is moderately to significantly weaker than $c + a$ slip on pyramidal planes. Thus, families with many grains well-oriented for low-*CRSS Pria* or *Baa* will be plastically "softer" than other families.

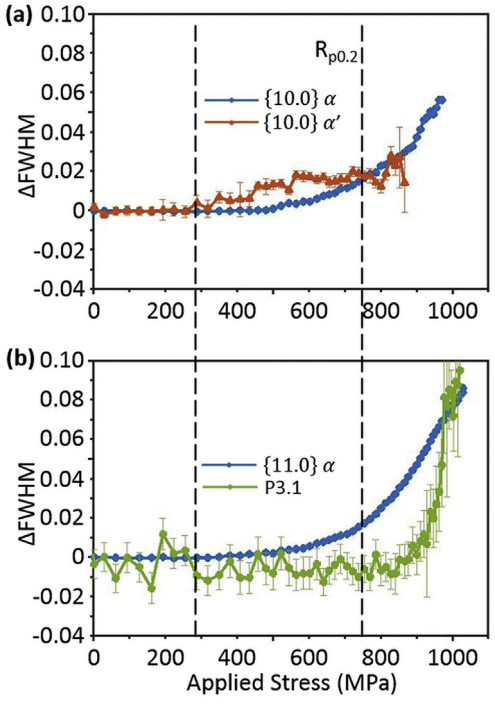

Fig. 6. Peak broadening of the (a) {11.0} and (b) {10.0} grain families in the 900C sample. The same stresses as in Fig. 5 are marked for comparison.

The Schmid Factor (SF) has been shown to be a relevant predictor of slip activity in a single Ti–6Al–4V crystallite once it has plastified [52]. However, each grain family consists of a wide range of crystallite orientations with respect to the loading direction. This is diagrammed for the {10.2} grain family as an example in Fig. 7a. Thus, the SF distribution for potentially active slip mechanisms is calculated for all possible orientations contributing to each grain family (Fig. 7b–e). The *CRSS* of each slip mechanism relative to $CRSS_{Pria}$ from crystal plasticity simulations [46,47] is shown in Fig. 7f. Only the highest SF from all possible slip systems is shown for each slip mechanism.

From Fig. 7, the {10.0} and {11.0} grain families likely contain a mix of plastically "soft" and "hard" grains. Grains with $\theta_{c-\text{axis}} < 25$ deg. are plastically hard, with SFs below 0.35 for all *a* -type slip mechanisms, and only grains with $\theta_{c-\text{axis}} > 45$ deg. (>60 deg. for {11.0}) deform by the slip mode with the lowest *CRSS*, *Pria* slip. The change in the XRD peak shows that the ensemble behavior of these grains takes load. Conversely, all grain orientations possibly contributing to the {20.3} and {10.2} (Fig. 6h and i) reflections are plastically soft (SF > 0.35 for either *Pria* or *Baa* slip in every grain), explaining the significant load-shedding observed in the families.

The load transfer trends observed between α, α', and Phase-3 for the 900C sample are also occurring in samples that underwent different heat treatments. The effect of the heat treatment on

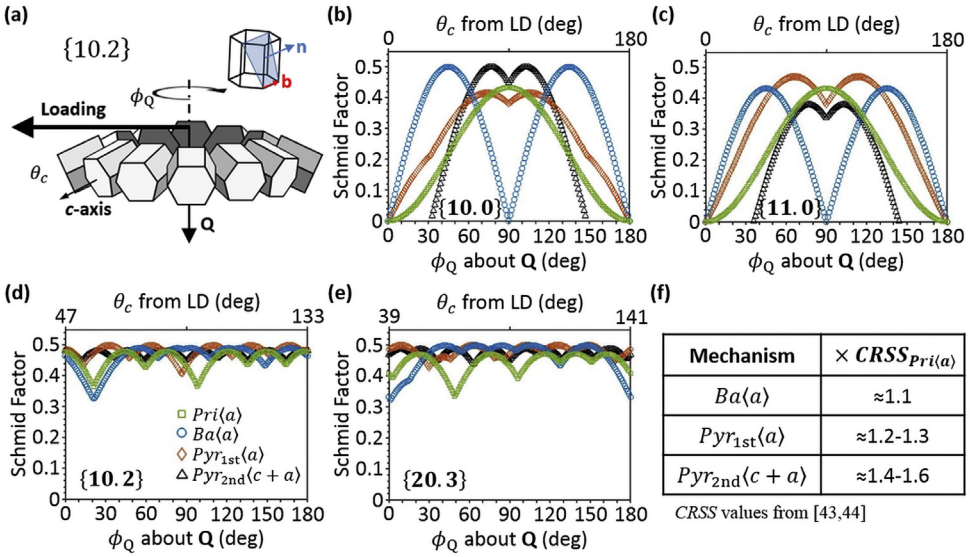

Fig. 7. (a) Schematic of possible crystallite orientations that contribute to the {10.2} grain family and their relationship to the loading direction and **Q**; (b–e) Maximum SF distributions for *Baa*, *Pria*, and $Pyr_{1st}a$ slip for all possible grain orientations contributing to the XRD signal for each grain family.

the mechanical properties will be described later, in Section 3.α 3.

3.2.2. Strain partitioning between phases: In situ HRDIC

In situ HRDIC was performed during interrupted tensile loading of dogbones treated at 900C to further understand the strain partitioning between the phases. The strain maps from an OPS-speckled sample are shown in Fig. 8. The boundaries between the α lamellae and martensite regions have been highlighted in black. The maps show that strain is accommodated primarily by the martensite regions early in the deformation (Fig. 8b–d), as expected from the XRD (Fig. 8b–f). The strain in the martensite is distributed throughout the regions. However, it is not homogeneous but instead localized at the interfaces between the α lamellae and martensite regions. By contrast, strain within a single α lamella is not homogeneously distributed but instead localized in planar slip bands.

In situ HRDIC was also performed on a gold-speckled sample to capture more details on the deformation behavior at a higher magnification. In Fig. 9, four adjacent strain maps have been stitched together to show a larger area. Arrows in the BSE micrograph (Fig. 9a) indicate four particularly large laths in the martensite region. The local strain evolution in the martensite regions described in Fig. 9 appears much less homogeneous than what was observed in the OPS-speckled map. High strain concentrations are observed at α grain boundaries because of the strain mismatch between the $\varepsilon_{pl} = 0.82\%$ lamellae and martensite regions. Strain appears to accumulate preferentially at lamellae oriented near 45° to the loading direction.

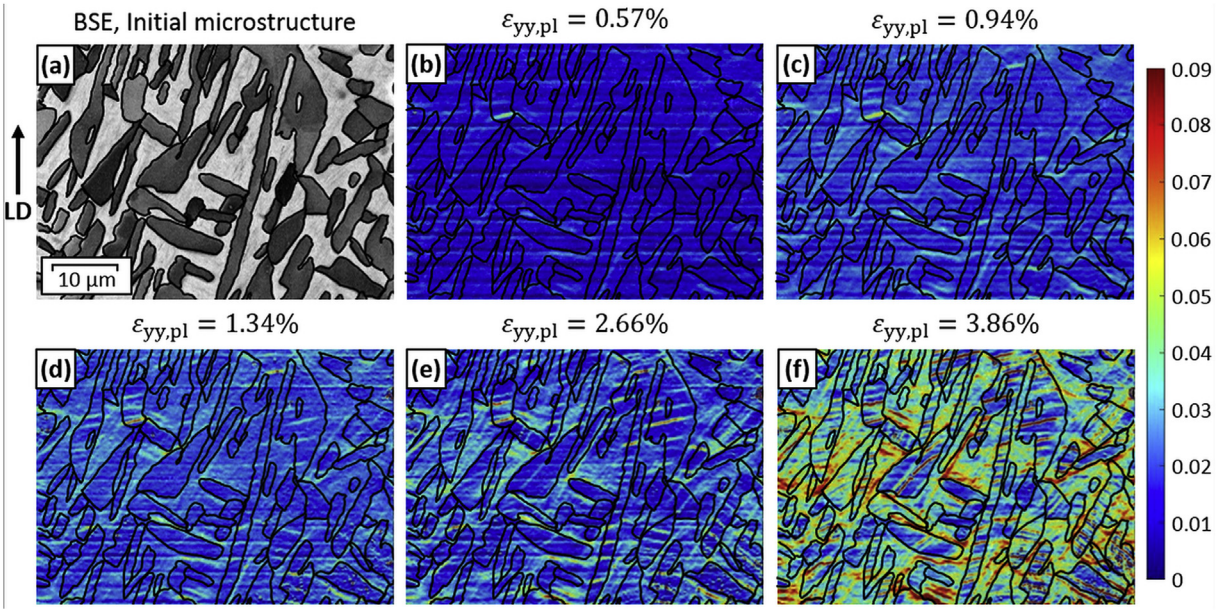

Fig. 8. (a) BSE micrograph of the initial microstructure with α lamellae (dark grey) surrounded by martensite regions (light grey); (b)–(f) HRDIC strain maps at various stages of loading. Approximate locations of the grain boundaries have been highlighted in black.

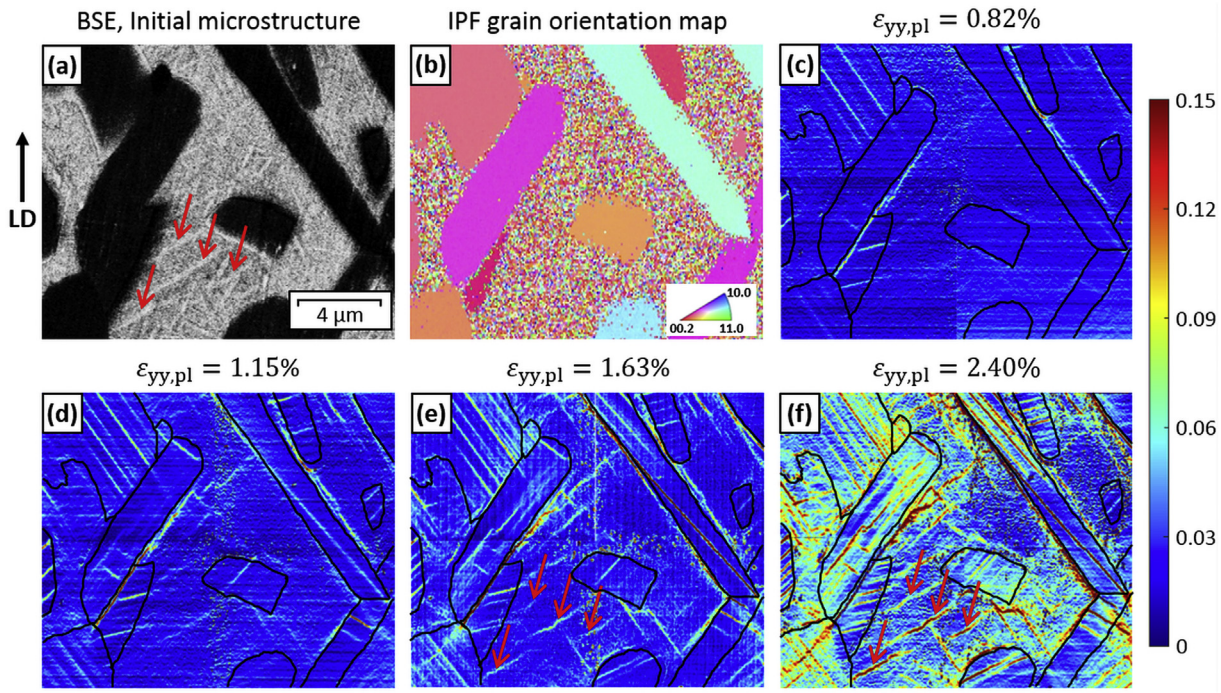

Fig. 9. (a) BSE micrograph of the initial microstructure with α lamellae (dark grey) surrounded by martensite regions (light grey); (b) IPF map of the examined region; (c)–(f) HRDIC strain maps at various stages of loading.

By α, slip bands appear already in several $\varepsilon_{pl} = 01.63\%$ lamellae (Fig. 9c). Between $\varepsilon_{pl} = 2.40\%$ (Fig. 9e) and (Fig. 9f), very few new slip bands are forming. Instead, existing slip bands grow and intensify, as in grain 9. This implies that dislocations are nucleating and gliding on slip planes which are already active. The single slip-dominated behavior of the α phase has been previously documented in Ti alloys and the active slip mechanism is shown to be well-predicted by SF analysis [52–54]. Slip trace analysis of the strain maps confirms that low-CRSS *Pria* and *Baa* slip account for the majority of the slip traces.

Within the martensite region, strain localizations appear along interfaces of several martensite laths (marked by arrows in Fig. 9e). Strain accumulates preferentially at the larger laths, in particular with their major axis oriented near 45° to the loading direction. The intensity of these concentrations increases rapidly with increasing load and can be a source for the nucleation and growth of microcracks within the martensite regions.

3.2.3. Post-mortem electron microscopy characterization

TEM micrographs of the deformed 980C sample are shown in Fig. 10a–c. The 980C sample is shown because it had particularly large α' laths that could be examined for the dislocation structure. Only a single active slip system is observed in the α lamellae, shown in Fig. 10b. The dislocations are more densely packed at the grain boundary than at the center of the grain, suggesting that they are nucleating from the interface and travelling into the grain [55]. The pile-up of these dislocations are responsible for the very localized strain bands observed in the HRDIC (Figs. 8 and 10). By contrast, a forest of dislocations is observed in the α' lath (Fig. 10c) typical of high work hardening materials. The α' lath contains several twins which are suspected to have formed during the $\beta \rightarrow \alpha'$ martensite transformation [19].

The TEM observations in Fig. 10a–c suggest that slip transmission between the martensite regions and the α lamellae hardly occurs. Only in cases where 1) the width of the martensite region between adjacent α lamellae is narrow and 2) these lamellae have the same crystallographic orientation, shearing can occur across the martensite regions. This is seen in electron contrast channelling imaging (ECCI) micrograph of the deformed 900C sample in Fig. 10d.

3.3. The role of the heat treatment temperature

The qualitative trends presented for the 900C sample are consistent for all heat treatments. However, the yield stress and work hardening of the grain families varies with heat treatment (Fig. 3). The elastic lattice strain evolutions of the {10.0} α and α' and the {11.0} α and P3.1 grain families for all heat treatments are shown in Fig. 11. The slightly different behavior of the {10.0} α peak in the 950C sample compared to the other heat treatments is probably a fitting artefact due to the overlap of a low intensity Phase-3 peak with {10.0} α. As the annealing temperature and thus martensite region volume fraction increases, the following trends can be observed:

(1) The yield strength of all phases increases. For every 5% increase in martensite ($\alpha' + Phase-3$) vol. fract., the yield strength of the α lamellae increases ~30 MPa and that of the α' laths increases ~60 MPa.
(2) The macroscopic applied stress at which Phase-3 sheds load seems to be independent of heat treatment. The width of the P3.1 peak stays relatively constant up to $R_{p0.2}$, implying that the phase is not plastifying but instead shedding load due to delamination between the martensite regions and the α lamellae.

The primary effect of annealing at different sub- β transus temperatures is to change the volume fraction and chemical composition of the phases. Chemical partitioning of solute elements Al and V decreases with annealing temperature. Thus, after

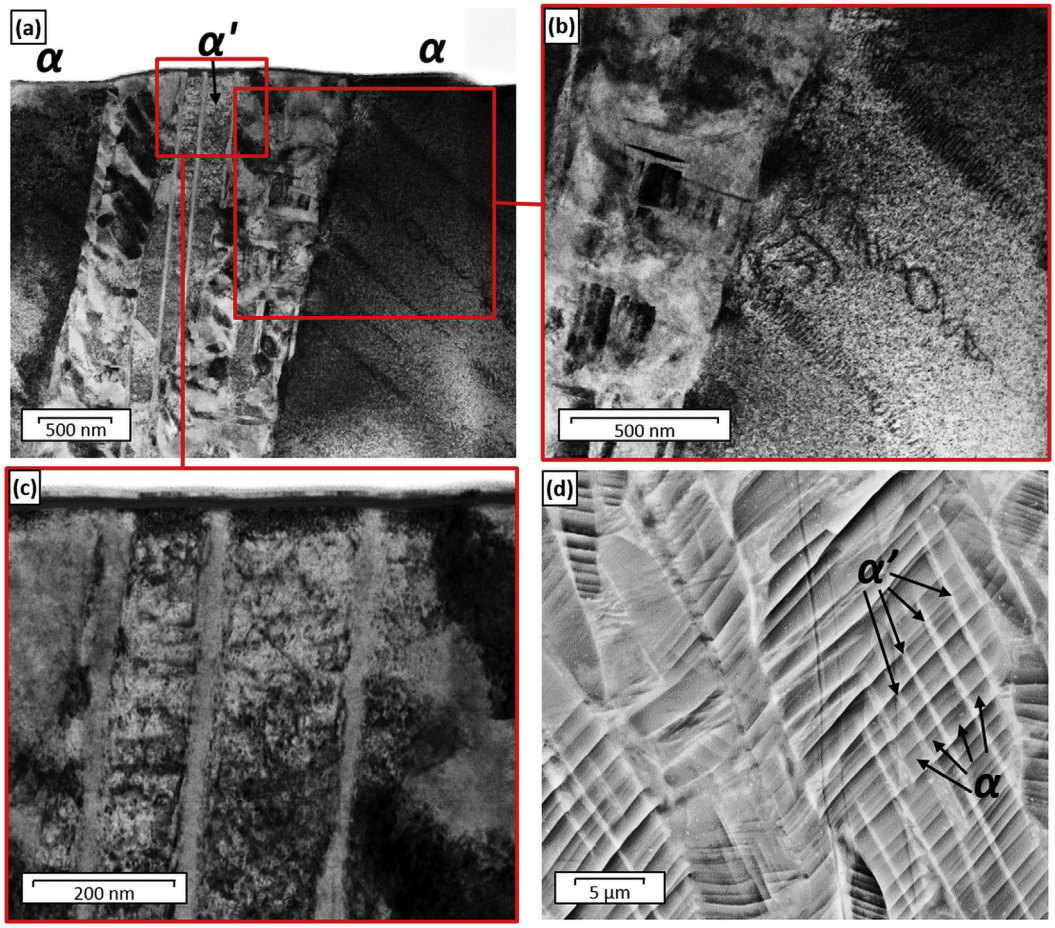

Fig. 10. (a) TEM micrograph of the 980C sample after 12% strain; (b) Magnified view of forest dislocation structure in a large α' lath; (c) Magnified view of dislocation pileups on single slip systems at the interfaces of an α lamella; (d) ECCI image of the 900C sample after 5% strain.

the quench, there is a higher concentration of Al in α' at higher annealing temperatures [56]. Al is the primary solid solution strengthening element for Ti–6Al–4V [57,58] and can explain the observed increase in the yield strength of the α' phase. The higher annealing temperatures also result in a larger volume fraction of the martensite regions. The combination of these two effects result in more load being taken by the martensite regions and less load being felt by the α lamellae. Thus, it takes a higher applied stress to cause yield in the α lamellae. The result is that the macroscopic yield stress increases as the annealing temperature is increased.

4. Discussion

The mechanical properties of the EBM + heat-treated Ti–6Al–4V come from the synergistic behavior between three mechanically distinct phases: α lamellae and a composite martensite region consisting of laths of α' and a third hard phase. The enhanced work hardening can be attributed to a progressive load sharing and plasticity of the phases. The findings are summarized below:

1. **Below 300 MPa**, the linear evolution of the elastic lattice strains suggest all phases are deforming elastically.
2. **Between 300 MPa (~0.4$R_{p0.2}$) and $R_{p0.2}$=760 MPa**, the elastic lattice strains show that the martensite composite takes less load compared to the elastic region. HRDIC shows that strain is inhomogeneously accommodated in the martensite regions and large strain mismatches develop at the interfaces of α lamellae and martensite regions $(\alpha' + Phase-3)$, suggesting local delamination. The α' laths begin to plastify, resulting in peak broadening, while the P3.1 peak width stays relatively constant, suggesting that the phase has not begun to plastify yet. The lattice strain evolution of the α lamellae deviates slightly from linearity suggesting that a few well-oriented grains begin to plastify. This also results in a slight peak broadening. The collective behavior of the three phases results in high work hardening rates at low strains.
3. **Above $R_{p0.2}$=760 MPa**, the elastic lattice strains show that plastically soft α grain families begin shedding load, which is redistributed to the harder α grain families and Phase-3. The latter behaves as the hardest phase and takes significant load as shown in Fig. 11. Work hardening in the sample comes from the pile-up of dislocations in the α lamellae. The sudden increase in FWHM of P3.1 (Fig. 6) suggests Phase-3 deforms or comes under a huge intergranular stress. In this regime, strain localizations develop within the martensite at the interfaces of the larger laths. These strain localizations can eventually lead to crack propagation and failure.
4. As annealing temperature increases, the macroscopic yield stress and UTS increase, which can be explained by the higher volume fractions of martensite $(\alpha' + Phase-3)$ which takes more load and delays the onset of plasticity in the α lamellae.
5. For every 5% increase in martensite region volume fraction, the yield strength of the α lamellae and α' laths increases ~30 MPa and ~60 MPa, respectively.

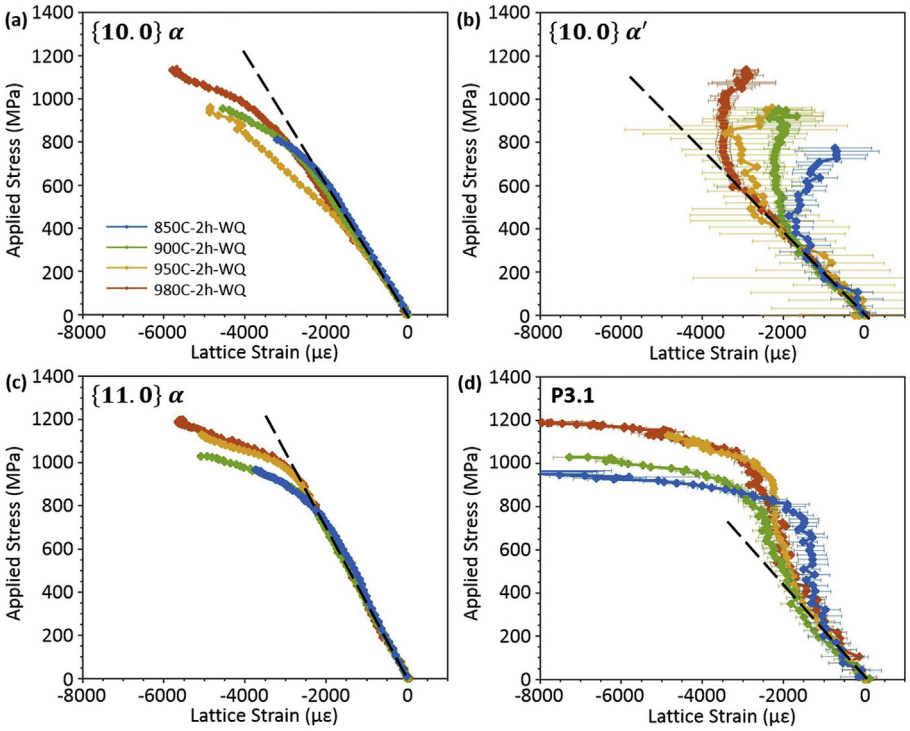

Fig. 11. Elastic lattice strain evolution of the (a) {11.0} and (b) {10.0} grain families for all heat treated samples. The dashed black lines serve as a guide for the eye.

The 850C and 900C samples have yield strengths lower than that of the as-HIP'ed (Fig. 3a). This was also noted in Ref. [18] where it was proposed to be due to the presence of soft α'' martensite, although the phase was not observed. Our findings suggest that the yield strength is related to the plastic yield of the α lamellae that results from the early load shedding of the martensite regions $(\alpha' + \ Phase-3)$, where the α' martensite behaves plastically soft. At lower annealing temperatures, the martensite regions transfer load earlier to the α lamellae, causing the lower yield stress of the α phase and thus lower macroscopic yield stress.

4.1. Mechanically hard behavior of Phase-3

As mentioned earlier, Phase-3 can be indexed as either OR or HCP. The SAED from selected laths shows a better fit for OR, suggesting that Phase-3 is α'' martensite. However, α'' martensite is conventionally considered a "soft" phase with low yield strength and high ductility [45]. XRD observations of Ti–7%Mo (wt.) by Ivasishin et al. [59] showed that α'' peaks merged into a single peak after deformation, suggesting that soft behavior of the martensite is due to the transformation of the OR structure to an HCP structure. Our *in situ* XRD observations, however, show distinct Phase-3 peaks throughout the deformation so there is no evidence for such a transformation. OR phases in other materials have been shown to be plastically hard, such as cementite particles in bainitic steel [60], but such behavior has never been reported for α'' martensite in Ti alloys.

Conversely, considering Phase-3 as a third HCP phase, then the hard mechanical behavior could then be explained by the large lattice parameters and the small size of the laths. Compared to the α and α' phases, Phase-3 would have the largest *a* lattice parameter. The low-CRSS deformation mechanisms of Ti–6Al–4V involve *a* slip on basal and prismatic planes, which would be hindered by the larger *a* lattice parameter. Additionally, the Phase-3 laths are approximately one order of magnitude smaller than the α lamellae, which would lead to an additional Hall-Petch hardening effect compared to the primary α phase.

Regardless of its structure, the presence of an additional hard phase plays a key role in the enhanced ductility in the 980C sample and in the materials prepared by de Formanoir et al. [18]. Previously, Matsumoto et al. [25] were able to achieve UTS > 1200 MPa and elongation before failure of ~14% in a dual-phase $\alpha + \alpha'$ Ti-6AL-4V. They attribute the enhanced ductility to the reduced strain incompatibility and increased slip transmission between two HCP phases, which allows the sample to strain without a significant work hardening after 1–2% plastic strain. Conversely, the work hardening in this study and observed by de Formanoir et al. in Ref. [18] remains relatively high over the entire deformation and there is no evidence that slip transfer occurs between the martensite and α grains. In this regime the lattice strains show that Phase-3 shares load with the α grains, which allows the α lamellae to continue to deform and work harden.

5. Conclusion

The origin of a high work hardening in Ti–6Al–4V alloys prepared by EBM was characterized using *in situ* XRD and HRDIC. Samples were post-treated with a sub- β transus anneal followed by water quenching (described in Ref. [18]) to produce a microstructure of α lamellae surrounded by regions of martensite. The martensite regions are shown to have a composite structure due to the presence of a third, hard phase previously unidentified in this material. The enhanced work hardening and extended plasticity is explained by a gradual load transfer between the three phases: load transfer from the α lamellae to the martensitic regions and load transfer between the two phases present in the martensitic region. Strain partitioning is inhomogeneous at the micro scale and delamination between the three phases is observed which will eventually lead to failure.

Acknowledgements

This work was supported by the European Research Council within the ERC Advanced Grant MULTIAX (339245). The authors would like to gratefully acknowledge the ERC for their financial support. The authors would also like to acknowledge the Ministry of Education, Youth, and Sports of the Czech Republic for financial support and use of research equipment and infrastructure under the project m-0IPMinfra (CZ.02.1.01/0.0/0.0/16_013/0001823). The authors would also like to acknowledge Dr. Steven Van Petegem for his aid and support during in-situ XRD measurements.

Appendix A. Supplementary data

Supplementary data to this article can be found online at https://doi.org/10.1016/j.actamat.2019.08.037.

References

[1] O.L.A. Harrysson, O. Cansizoglu, D.J. Marcellin-Little, D.R. Cormier, H.A. West, Direct metal fabrication of titanium implants with tailored materials and mechanical properties using electron beam melting technology, Mater. Sci. Eng. C 28 (2008) 366–373, https://doi.org/10.1016/j.msec.2007.04.022.

[2] L.E. Murr, S.A. Quinones, S.M. Gaytan, M.I. Lopez, A. Rodela, E.Y. Martinez, D.H. Hernandez, E. Martinez, F. Medina, R.B. Wicker, Microstructure and mechanical behavior of Ti–6Al–4V produced by rapid-layer manufacturing, for biomedical applications, J. Mech. Behav. Biomed. Mater. 2 (2009) 20–32, https://doi.org/10.1016/j.jmbbm.2008.05.004.

[3] D. Banerjee, J.C. Williams, Perspectives on titanium science and technology, Acta Mater. 61 (2013) 844–879, https://doi.org/10.1016/j.actamat.2012.10.043.

[4] M. Qian, W. Xu, M. Brandt, H.P. Tang, Additive manufacturing and post-processing of Ti-6Al-4V for superior mechanical properties, MRS Bull. 41 (2016) 775–784, https://doi.org/10.1557/mrs.2016.215.

[5] M. Peters, J. Kumpfert, C.H. Ward, C. Leyens, Titanium alloys for aerospace applications, Adv. Eng. Mater. 5 (2003) 419–427, https://doi.org/10.1002/adem.200310095.

[6] S. Ford, Additive Manufacturing Technology: Potential Implications for U.S. Manufacturing Competitiveness, Social Science Research Network, Rochester, NY, 2014. https://papers.ssrn.com/abstract=2501065. (Accessed 13 November 2018).

[7] K. Wang, The use of titanium for medical applications in the USA, Mater. Sci. Eng., A 213 (1996) 134–137, https://doi.org/10.1016/0921-5093(96)10243-4.

[8] M. Niinomi, Mechanical properties of biomedical titanium alloys, Mater. Sci. Eng., A 243 (1998) 231–236, https://doi.org/10.1016/S0921-5093(97)00806-X.

[9] C. de Formanoir, G. Martin, F. Prima, S.Y.P. Allain, T. Dessolier, F. Sun, S. Vivès, B. Hary, Y. Bréchet, S. Godet, Micromechanical behavior and thermal stability of a dual-phase α+α' titanium alloy produced by additive manufacturing, Acta Mater. 162 (2019) 149–162, https://doi.org/10.1016/j.actamat.2018.09.050.

[10] G. Lütjering, Influence of processing on microstructure and mechanical properties of (α+β) titanium alloys, Mater. Sci. Eng., A 243 (1998) 32–45, https://doi.org/10.1016/S0921-5093(97)00778-8.

[11] S. Bruschi, S. Poggio, F. Quadrini, M.E. Tata, Workability of Ti–6Al–4V alloy at high temperatures and strain rates, Mater. Lett. 58 (2004) 3622–3629, https://doi.org/10.1016/j.matlet.2004.06.058.

[12] Y. Long, T. Wang, H.Y. Zhang, X.L. Huang, Enhanced ductility in a bimodal ultrafine-grained Ti–6Al–4V alloy fabricated by high energy ball milling and spark plasma sintering, Mater. Sci. Eng., A 608 (2014) 82–89, https://doi.org/10.1016/j.msea.2014.04.057.

[13] S. Zherebtsov, E. Kudryavtsev, S. Kostjuchenko, S. Malysheva, G. Salishchev, Strength and ductility-related properties of ultrafine grained two-phase titanium alloy produced by warm multiaxial forging, Mater. Sci. Eng., A 536 (2012) 190–196, https://doi.org/10.1016/j.msea.2011.12.102.

[14] Y. Chong, T. Bhattacharjee, M.-H. Park, A. Shibata, N. Tsuji, Factors determining room temperature mechanical properties of bimodal microstructures in Ti-6Al-4V alloy, Mater. Sci. Eng., A 730 (2018) 217–222, https://doi.org/10.1016/j.msea.2018.06.019.

[15] S. Hémery, V.T. Dang, L. Signor, P. Villechaise, Influence of microtexture on early plastic slip activity in Ti-6Al-4V polycrystals, Metall. Mater. Trans. A 49 (2018) 2048–2056, https://doi.org/10.1007/s11661-018-4569-4.

[16] H. Galarraga, R.J. Warren, D.A. Lados, R.R. Dehoff, M.M. Kirka, P. Nandwana, Effects of heat treatments on microstructure and properties of Ti-6Al-4V ELI alloy fabricated by electron beam melting (EBM), Mater. Sci. Eng. A 685 (2017) 417–428, https://doi.org/10.1016/j.msea.2017.01.019.

[17] J. Yao, T. Suo, S. Zhang, F. Zhao, H. Wang, J. Liu, Y. Chen, Y. Li, Influence of heat-treatment on the dynamic behavior of 3D laser-deposited Ti–6Al–4V alloy, Mater. Sci. Eng., A 677 (2016) 153–162, https://doi.org/10.1016/j.msea.2016.09.036.

[18] C. de Formanoir, A. Brulard, S. Vivès, G. Martin, F. Prima, S. Michotte, E. Rivière, A. Dolimont, S. Godet, A strategy to improve the work-hardening behavior of Ti–6Al–4V parts produced by additive manufacturing, Mater. Res. Lett. 5 (2017) 201–208, https://doi.org/10.1080/21663831.2016.1245681.

[19] G. Ter Haar, T. Becker, G.M. Ter Haar, T.H. Becker, Selective laser melting produced Ti-6Al-4V: post-process heat treatments to achieve superior tensile properties, Materials 11 (2018) 146, https://doi.org/10.3390/ma11010146.

[20] B. Vrancken, L. Thijs, J.-P. Kruth, J. Van Humbeeck, Heat treatment of Ti6Al4V produced by selective laser melting: microstructure and mechanical properties, J. Alloy. Comp. 541 (2012) 177–185, https://doi.org/10.1016/j.jallcom.2012.07.022.

[21] G. Kasperovich, J. Hausmann, Improvement of fatigue resistance and ductility of TiAl6V4 processed by selective laser melting, J. Mater. Process. Technol. 220 (2015) 202–214, https://doi.org/10.1016/j.jmatprotec.2015.01.025.

[22] H.K. Rafi, N.V. Karthik, H. Gong, T.L. Starr, B.E. Stucker, Microstructures and mechanical properties of Ti6Al4V parts fabricated by selective laser melting and electron beam melting, J. Mater. Eng. Perform. 22 (2013) 3872–3883, https://doi.org/10.1007/s11665-013-0658-0.

[23] K. Wissenbach, S. Höges, P. Robotti, A. Molinari, L. Facchini, E. Magalini, Ductility of a Ti-6Al-4V alloy produced by selective laser melting of prealloyed powders, Rapid Prototyp. J. 16 (2010) 450–459, https://doi.org/10.1108/13552541011083371.

[24] A. Zafari, K. Xia, High Ductility in a fully martensitic microstructure: a paradox in a Ti alloy produced by selective laser melting, Mater. Res. Lett. 6 (2018) 627–633, https://doi.org/10.1080/21663831.2018.1525773.

[25] H. Matsumoto, H. Yoneda, K. Sato, S. Kurosu, E. Maire, D. Fabregue, T.J. Konno, A. Chiba, Room-temperature ductility of Ti–6Al–4V alloy with α′ martensite microstructure, Mater. Sci. Eng., A 528 (2011) 1512–1520, https://doi.org/10.1016/j.msea.2010.10.070.

[26] H. Matsumoto, K. Kodaira, K. Sato, T.J. Konno, A. Chiba, Microstructure and mechanical properties of α′ martensite type Ti alloys deformed under the α′ processing, Mater. Trans. 50 (2009) 2744–2750, https://doi.org/10.2320/matertrans.MA200912.

[27] P.R. Willmott, D. Meister, S.J. Leake, M. Lange, A. Bergamaschi, M. Böge, M. Calvi, C. Cancellieri, N. Casati, A. Cervellino, Q. Chen, C. David, U. Flechsig, F. Gozzo, B. Henrich, S. Jäggi-Spielmann, B. Jakob, I. Kalichava, P. Karvinen, J. Krempasky, A. Lüdeke, R. Lüscher, S. Maag, C. Quitmann, M.L. Reinle-Schmitt, T. Schmidt, B. Schmitt, A. Streun, I. Vartiainen, M. Vitins, X. Wang, R. Wullschleger, The materials science beamline upgrade at the Swiss light source, J. Synchrotron Radiat. 20 (2013) 667–682, https://doi.org/10.1107/S0909049513018475.

[28] O. Muránsky, D.G. Carr, M.R. Barnett, E.C. Oliver, P. Šittner, Investigation of deformation mechanisms involved in the plasticity of AZ31 Mg alloy: in situ neutron diffraction and EPSC modelling, Mater. Sci. Eng., A 496 (2008) 14–24, https://doi.org/10.1016/j.msea.2008.07.031.

[29] D. Yan, C.C. Tasan, D. Raabe, High resolution in situ mapping of microstrain and microstructure evolution reveals damage resistance criteria in dual phase steels, Acta Mater. 96 (2015) 399–409, https://doi.org/10.1016/j.actamat.2015.05.038.

[30] W.-N. Hsu, E. Polatidis, M. Šmíd, N. Casati, S. Van Petegem, H. Van Swygenhoven, Load path change on superelastic NiTi alloys: in situ synchrotron XRD and SEM DIC, Acta Mater. 144 (2018) 874–883, https://doi.org/10.1016/j.actamat.2017.11.035.

[31] F. Di Gioacchino, J. Quinta da Fonseca, Plastic strain mapping with sub-micron resolution using digital image correlation, Exp. Mech. 53 (2013) 743–754, https://doi.org/10.1007/s11340-012-9685-2.

[32] S.V. Petegem, A. Guitton, M. Dupraz, A. Bollhalder, K. Sofinowski, M.V. Upadhyay, H.V. Swygenhoven, A miniaturized biaxial deformation rig for in situ mechanical testing, Exp. Mech. 57 (2017) 569–580, https://doi.org/10.1007/s11340-016-0244-0.

[33] J. Blaber, B. Adair, A. Antoniou, Ncorr: open-source 2D digital image correlation Matlab software, Exp. Mech. 55 (2015) 1105–1122, https://doi.org/10.1007/s11340-015-0009-1.

[34] J.L.W. Carter, M.D. Uchic, M.J. Mills, Impact of speckle pattern parameters on DIC strain resolution calculated from in-situ SEM experiments, in: J. Carroll, S. Daly (Eds.), Fracture, Fatigue, Failure, and Damage Evolution, vol. 5, Springer International Publishing, 2015, pp. 119–126.

[35] S.S. Al-Bermani, M.L. Blackmore, W. Zhang, I. Todd, The origin of microstructural diversity, texture, and mechanical properties in electron beam melted Ti-6Al-4V, Metall. Mater. Trans. A 41 (2010) 3422–3434, https://doi.org/10.1007/s11661-010-0397-x.

[36] A. Safdar, L.-Y. Wei, A. Snis, Z. Lai, Evaluation of microstructural development in electron beam melted Ti-6Al-4V, Mater. Char. 65 (2012) 8–15, https://doi.org/10.1016/j.matchar.2011.12.008.

[37] M. Simonelli, Y.Y. Tse, C. Tuck, On the texture formation of selective laser melted Ti-6Al-4V, Metall. Mater. Trans. A 45 (2014) 2863–2872, https://doi.org/10.1007/s11661-014-2218-0.

[38] J. Ahn, E. He, L. Chen, R.C. Wimpory, J.P. Dear, C.M. Davies, Prediction and measurement of residual stresses and distortions in fibre laser welded Ti-6Al-4V considering phase transformation, Mater. Des. 115 (2017) 441–457, https://doi.org/10.1016/j.matdes.2016.11.078.

[39] Q. Chen, L. Liu, C. Zhu, K. Chen, Mesomechanical modeling and numerical simulation of the diffraction elastic constants for Ti6Al4V polycrystalline alloy, Metals 8 (2018) 822, https://doi.org/10.3390/met8100822.

[40] T. Ahmed, H.J. Rack, Phase transformations during cooling in α+β titanium

alloys, Mater. Sci. Eng. A 243 (1998) 206–211, https://doi.org/10.1016/S0921-5093(97)00802-2.
[41] X. Tan, Y. Kok, W.Q. Toh, Y.J. Tan, M. Descoins, D. Mangelinck, S.B. Tor, K.F. Leong, C.K. Chua, Revealing martensitic transformation and α/β interface evolution in electron beam melting three-dimensional-printed Ti-6Al-4V, Sci. Rep. 6 (2016), 26039, https://doi.org/10.1038/srep26039.
[42] D. Raabe, S. Sandlöbes, J. Millán, D. Ponge, H. Assadi, M. Herbig, P.-P. Choi, Segregation engineering enables nanoscale martensite to austenite phase transformation at grain boundaries: a pathway to ductile martensite, Acta Mater. 61 (2013) 6132–6152, https://doi.org/10.1016/j.actamat.2013.06.055.
[43] D. Raabe, M. Herbig, S. Sandlöbes, Y. Li, D. Tytko, M. Kuzmina, D. Ponge, P.-P. Choi, Grain boundary segregation engineering in metallic alloys: a pathway to the design of interfaces, Curr. Opin. Solid State Mater. Sci. 18 (2014) 253–261, https://doi.org/10.1016/j.cossms.2014.06.002.
[44] M. Kuzmina, M. Herbig, D. Ponge, S. Sandlöbes, D. Raabe, Linear complexions: confined chemical and structural states at dislocations, Science 349 (2015) 1080–1083, https://doi.org/10.1126/science.aab2633.
[45] G. Welsch, R. Boyer, E.W. Collings, Materials Properties Handbook: Titanium Alloys, ASM International, 1993.
[46] F. Bridier, D.L. McDowell, P. Villechaise, J. Mendez, Crystal plasticity modeling of slip activity in Ti–6Al–4V under high cycle fatigue loading, Int. J. Plast. 25 (2009) 1066–1082, https://doi.org/10.1016/j.ijplas.2008.08.004.
[47] J. Galan-Lopez, S. Naghdy, P. Verleysen, L.A.I. Kestens, F. Coghe, L. Rabet, J. Degrieck, Mechanical behavior and texture prediction of Ti-6Al-4V based on elastic viscoplastic self-consistent modelling, IOP Conf. Ser. Mater. Sci. Eng. 82 (2015), 012027, https://doi.org/10.1088/1757-899X/82/1/012027.
[48] I.P. Jones, W.B. Hutchinson, Stress-state dependence of slip in Titanium-6Al-4V and other H.C.P. metals, Acta Metall. 29 (1981) 951–968, https://doi.org/10.1016/0001-6160(81)90049-3.
[49] P.R. Dawson, D.E. Boyce, J.-S. Park, E. Wielewski, M.P. Miller, Determining the strengths of HCP slip systems using harmonic analyses of lattice strain distributions, Acta Mater. 144 (2018) 92–106, https://doi.org/10.1016/j.actamat.2017.10.032.
[50] M. Kasemer, M.P. Echlin, J.C. Stinville, T.M. Pollock, P. Dawson, On slip initiation in equiaxed α/β Ti-6Al-4V, Acta Mater. 136 (2017) 288–302, https://doi.org/10.1016/j.actamat.2017.06.059.
[51] X. Song, S.Y. Zhang, D. Dini, A.M. Korsunsky, Finite element modelling and diffraction measurement of elastic strains during tensile deformation of HCP polycrystals, Comput. Mater. Sci. 44 (2008) 131–137, https://doi.org/10.1016/j.commatsci.2008.01.043.
[52] F. Bridier, P. Villechaise, J. Mendez, Analysis of the different slip systems activated by tension in a α/β titanium alloy in relation with local crystallographic orientation, Acta Mater. 53 (2005) 555–567, https://doi.org/10.1016/j.actamat.2004.09.040.
[53] J.C. Williams, R.G. Baggerly, N.E. Paton, Deformation behavior of HCP Ti-Al alloy single crystals, Metall. Mater. Trans. A 33 (2002) 837–850, https://doi.org/10.1007/s11661-002-0153-y.
[54] S. Zaefferer, A study of active deformation systems in titanium alloys: dependence on alloy composition and correlation with deformation texture, Mater. Sci. Eng., A 344 (2003) 20–30, https://doi.org/10.1016/S0921-5093(02)00421-5.
[55] S. Han, P. Eisenlohr, M.A. Crimp, ECCI based characterization of dislocation shear in polycrystalline arrays during heterogeneous deformation of commercially pure titanium, Mater. Char. 142 (2018) 504–514, https://doi.org/10.1016/j.matchar.2018.06.003.
[56] R. Castro, L. Séraphin, Contribution à l'étude métallographique et structurale de l'alliage de titane TA6V, Les Mémoires Scientifiques de La Revue de Métallurgie. 63 (1966) 1025–1058.
[57] P. Kwasniak, H. Garbacz, K.J. Kurzydlowski, Solid solution strengthening of hexagonal titanium alloys: restoring forces and stacking faults calculated from first principles, Acta Mater. 102 (2016) 304–314, https://doi.org/10.1016/j.actamat.2015.09.041.
[58] G. Lütjering, J.C. Williams, Titanium, second ed., Springer-Verlag, Berlin Heidelberg, 2007. www.springer.com/de/book/9783540713975. (Accessed 12 November 2018).
[59] O.M. Ivasishin, R.V. Teliovich, Transformation plasticity in titanium alpha double prime martensite, J. Phys. IV France 11 (2001), https://doi.org/10.1051/jp4:2001421. Pr4-165-Pr4-172.
[60] M.A. Weisser, A.D. Evans, S. Van Petegem, S.R. Holdsworth, H. Van Swygenhoven, In situ room temperature tensile deformation of a 1% CrMoV bainitic steel using synchrotron and neutron diffraction, Acta Mater. 59 (2011) 4448–4457, https://doi.org/10.1016/j.actamat.2011.03.068.